

Molecular Line Profiles from Contracting Dense Cores

Steven W. Stahler¹ and Jeffrey J. Yen²

Sstahler@astro.berkeley.edu

ABSTRACT

We recently proposed that molecular cloud dense cores undergo a prolonged period of quasi-static contraction prior to true collapse. This theory could explain the observation that many starless cores exhibit, through their spectral line profiles, signs of inward motion. We now use our model, together with a publicly available radiative transfer code, to determine the emission from three commonly used species - N_2H^+ , CS, and HCN. A representative dense core of $3 M_\odot$ that has been contracting for 1 Myr has line profiles that qualitatively match the observed ones. In particular, optically thick lines have about the right degree of blue-red asymmetry, the empirical hallmark of contraction. The $J = 2 \rightarrow 1$ rotational transition of CS only attains the correct type of profile if the species is centrally depleted, as has been suggested by previous studies. These results support the idea that a slow, but accelerating, contraction leads to protostellar collapse. In the future, the kind of analysis presented here can be used to assign ages to individual starless cores.

Subject headings: ISM: clouds, kinematics and dynamics, molecules — stars: formation — line: profiles

1. Introduction

Over the last decade, astronomers have carefully scrutinized the large fraction of molecular cloud dense cores that contain no point sources of radiation, in order to understand more fully the onset of star formation. It was already established that the gross properties of these objects differ little from their counterparts with internal stars (Lee & Myers 1999), except perhaps for a mass that is slightly higher on average (Jijina, Myers, & Adams 1999, Fig. 3). More detailed spectroscopic studies of molecular line emission revealed that many starless cores exhibit signs of inward contraction (Williams et al. 1999; Lee, Myers, & Tafalla 1999; Gregersen & Evans 2000;

¹Astronomy Department, University of California, Berkeley, CA 94720

²Physics Department, Stanford University, Stanford, CA 94305

Lee, Myers, & Tafalla 2001; Schnee et al. 2007). The hallmark of this so-called infall signature is an asymmetric emission line, often with a self-absorption dip, that is skewed to the blue.

There is a variety of line profiles seen in dense cores, sometimes even in the same object, and the profile just described is by no means universal. It is preferentially found in starless cores with a higher central column density and optical depth (e.g. Lee, Myers, & Tafalla 1999; Gregersen & Evans 2000). Such cores also exhibit chemical abundances that differentiate them from lower-density objects (Crapsi et al. 2005; Keto & Caselli 2008). The kinematic signature is especially common in more evolved dense cores that contain Class 0 and Class I sources, i.e., very young, embedded stars (Myers, Evans, & Ohashi 2000). These facts, together with the simple and compelling infall interpretation of the asymmetric profiles (Myers et al. 1996), have convinced most researchers that we are witnessing a type of contraction that precedes the free-fall collapse onto a protostar. The contraction hypothesis is especially convincing for starless cores, where there is no possibility of confusion from stellar outflows.

What is the physical cause of this motion? The observed magnitude of the infall velocity is typically a few tenths of the sound speed. This finding rules out ambipolar diffusion as the underlying process, since the characteristic ion-neutral drift speed is much smaller (e.g. Ciolek & Basu 2001). Conversely, the subsonic level of the velocity, together with the statistical prevalence of starless cores (e.g. Forbrich et al. 2009), indicate that such objects are relatively long-lived (Kirk, Johnstone, & Di Francesco 2005), and thus are unlikely to be in a true state of collapse, as proposed by Keto & Field (2005).

In a recent contribution (Stahler & Yen 2009, hereafter Paper I) we introduced a new model for the contraction. Starless cores, like all self-gravitating objects, undergo bulk oscillations. Indeed, there are now several cases where spectroscopic observations indicate that such oscillations are occurring (Redman, Keto, & Rawlings 2006; Broderick et al. 2007; Velusamy et al. 2008). For an object that has evolved to the point of collapse, by whatever means, the frequency of the lowest normal mode vanishes. We studied, using perturbation theory, how a cloud subject to such a frozen (more commonly called ‘neutral’) mode slowly evolves toward full-blown collapse. We found that this previously unrecognized phase of quasi-static contraction lasts a considerable period (of order 10^6 yr), during which time the cloud attains internal speeds similar to those observed (see Fig. 4 of Paper I).

Encouraged by this result, we now seek to forge a stronger link to the observations. We calculate, using a publicly available radiative transfer code, the emitted line spectrum from our model cloud. We choose three molecules that are among the most commonly employed in the spectroscopic studies: N_2H^+ , CS, and HCN. Following the early surveys of Turner & Thaddeus (1977) and Womack, Ziurys, & Wyckoff (1992), N_2H^+ is often used as a tracer of dense, relatively quiescent cloud gas. Its rotational lines are optically thin in low-mass dense cores. Thus, they do not exhibit either self-absorption or blue-red asymmetry, but serve principally as a gauge of excitation temperature and as a comparison benchmark with lines that are sensitive to internal cloud motion.

The rotational lines of CS are often optically thick, and can have asymmetric profiles that have long been interpreted kinematically (Walker et al. 1986). On the other hand, the infall signature is relatively weak in starless cores, in part because the polar molecule CS is depleted at high density from the gas phase onto grain mantles (Bergin & Langer 1997). Finally, the $J = 1 \rightarrow 0$ rotational transition of HCN has the strongest infall signature of all, and the molecule appears to suffer little depletion (Aikawa et al, 2005; Sohn et al. 2007).

Although our model cloud is a highly idealized isothermal sphere, the results of this study further lend credence to the underlying dynamical picture. For a representative $3 M_{\odot}$ cloud that has been contracting for 1 Myr, we find that all the calculated line profiles resemble those observed, at least in an average sense. Interestingly, the CS profile is only acceptable once we include central depletion of the molecule. In Section 2 below, we first describe our implementation of the radiative transfer program. Section 3 then summarizes observations to date of the three molecules in starless dense cores. We describe, in Section 4, how the emergent line profiles alter when we change our physical input parameters. Judging from these trends, we then select a canonical model cloud and compare its emission spectrum to the available data. Finally, Section 5 discusses limitations of the dynamical theory and the prospects for improvement. We also indicate how the model, even in its current, simplified form, can be used to assign contraction ages to individual starless cores.

2. Calculating Line Emission

For each selected cloud model, we solve the equation of transfer numerically, using the code RATRAN (Hogerheijde & van der Tak 2000). The basic strategy underlying this code is to choose randomly a set of cells outside the cloud that generate photons. These photons propagate through the cloud interior, while the molecular level populations are temporarily held fixed. The statistical equilibrium of the levels is then solved separately, whereupon photon propagation is reinitiated. The accelerated lambda iteration scheme introduced by Rybicki & Hummer (1991) ensures rapid convergence of the radiation field and level populations. Treatment of non-isotropic scattering is cumbersome in this approach, so RATRAN does not include this effect. Such a simplification is acceptable in the infrared and millimeter regime of interest.

The code must be supplemented by tables of molecular data, containing energy levels, degeneracies, Einstein A-values, and collisional rate coefficients. Here, we utilized the Leiden Atomic and Molecular Database (LAMDA). Shöier et al. (2005) describe the construction of the database and its use. These tables include the full multiplets of rotational lines created by hyperfine splitting. In fact, recent observational studies of dense core kinematics have focused on individual hyperfine lines, as we will describe.

In order to display the line spectra, we utilized the MIRIAD software package (Sault, Teuben, & Wright 1995). We placed our cloud at a representative distance of 140 pc, and “observed” it with a Gaussian beam of angular size $60''$. For comparison, our canonical cloud has a physical diameter of

0.27 pc, or 392'' at the selected distance. In constructing spectra, we assumed a velocity resolution of 0.01 km s⁻¹.

We tested the radiative transfer calculation by first reproducing prior results for line profiles in a collapsing cloud. An early and influential work was that of Zhou (1992). This study compared the self-similar collapse models of Shu (1977) with that derived independently by Larson (1969) and Penston (1969). Zhou (1992) calculated, for both models, CS rotational line profiles at various times, both before and after formation of the central protostar.¹

In testing both self-similar collapse models, Zhou (1992) assumed a gas kinetic temperature of 10 K. Following Lizano & Shu (1989), he augmented the Shu model with a turbulent velocity of the form

$$v_{\text{turb}} = \sqrt{\kappa/\rho}, \quad (1)$$

where κ is a constant and ρ is the local cloud density. The constant was determined empirically by Myers & Goodman (1988) to have the value $\kappa = 1.1 \times 10^{-11}$ g cm⁻¹ s⁻². Zhou (1992) argued that this figure was likely to be an overestimate, since the observed “turbulence” could have included infall motion for dense cores containing stars. Accordingly, he used a value of κ smaller by a factor of 0.25. Finally, he set the CS abundance, i.e., the number density of the molecule relative to hydrogen, to 4×10^{-9} , following Fuller (1989).

We provisionally adopted the same assumptions as Zhou (1992) and recalculated, using RATRAN, CS line profiles from the Shu model for the period after protostar formation. All lines were viewed through the cloud center. The RATRAN code allows one to select N_{tot} , the total number of shells in the cloud, as well as $r_{\text{out}}/r_{\text{in}}$, the ratio of outer to inner shell radii. We adjusted both numbers until we obtained the best match with the $J = 1 \rightarrow 0$, $J = 2 \rightarrow 1$, and $J = 3 \rightarrow 2$ profiles shown in Figure 3d of Zhou (1992). By choosing $N = 100$ and $r_{\text{out}}/r_{\text{in}} = 500$, we obtained an excellent fit to all profiles for the four times considered by Zhou (1992). Agreement did not improve when either N_{tot} or $r_{\text{out}}/r_{\text{in}}$ was increased further. For example, the peak antenna temperatures T_A changed by less than 0.1 %. We therefore retained these values of N_{tot} and $r_{\text{out}}/r_{\text{in}}$ in our subsequent calculations.

Turning to starless dense cores, we continued to use a gas kinetic temperature of 10 K, corresponding to a thermal speed of $a_T = 0.2$ km s⁻¹. This temperature is on the low end of the range found empirically by Jijina, Myers, & Adams (1999, Figure 2). In any case, it is important to note that purely thermal line profiles are never seen, even at the centers of the most quiescent objects (Barranco & Goodman 1998), and the prescription for turbulence in equation (1) continues to provide a useful representation of the observations. In light of the comments by Zhou (1992), we view

¹The original Larson-Penston model only considered collapse up to the point of protostar formation. Zhou (1992) utilized the calculation of Hunter (1977) to extend the flow past this point. Conversely, Shu (1977) only considered times *after* protostar formation. For the earlier epoch, Zhou (1992) employed a sequence of hydrostatic spheres of increasing central density.

κ as a free parameter, whose upper limit is likely to be the value advocated by Myers & Goodman (1988). It is straightforward to incorporate turbulence into RATRAN, which allows a variable degree of intrinsic line broadening in each mass shell of the cloud.

An additional free parameter is inherent in the theoretical model of Paper I. We envisioned the cloud undergoing a global oscillation, characterized by a nondimensional amplitude ϵ . For our standard initial conditions, ϵ gives the fractional deviation of the density from its unperturbed, equilibrium distribution (see eq. (17) and the discussion in §4.2). The numerical integration of Paper I used a relatively large amplitude of $\epsilon = 0.2$, motivated by observation and analysis of the starless core B68 (Keto et al. 2006). Here, we reset ϵ to the more modest, and perhaps more typical, value of 0.1. We comment later on how changing ϵ affects the emergent line profiles.

With these assumptions, the only remaining free parameters are the cloud mass M and the time of observation t . The zero point for t is the onset of quasi-static contraction. Both quantities must be related to the corresponding nondimensional ones, \tilde{M} and \tilde{t} , used in Paper I. Our model cloud has a fixed nondimensional mass, $\tilde{M} = 4.19$, where the number results from numerical integration of the isothermal Lane-Emden equation. Combining equation (9) and (12) of Paper I, we find that \tilde{M} and \tilde{t} are related by

$$\tilde{t} = \frac{\tilde{M} a_T^3 t}{GM}. \quad (2)$$

Since \tilde{M} and a_T are either known or preset, the equation tells us, for any M and t , the appropriate \tilde{t} to use from the model sequence. We further read off, at this point in the sequence, the distribution of the nondimensional density and velocity as functions of radius. The equations of §2.2 in Paper I tell us how to translate the quantities into dimensional form.²

3. Observations of the Molecules

3.1. N₂H⁺

After surveys had established the presence of N₂H⁺ in star-forming regions, targeted observations were pursued in dense cores, including those already detected in NH₃ (Caselli, Myers, & Thaddeus 1995; Benson, Caselli, & Myers 1998; Caselli et al. 2002). It was found that the molecule selectively traces dense and quiescent gas, and is indeed absent in hotter and shocked material. The $J = 1 \rightarrow 0$ rotational transition, which has 7 hyperfine components, is usually optically thin in starless cores, but not always so. For example, the well-studied core L1544 shows an asymmetric profile toward the cloud center, extending over a region some 1400 AU in radius (Tafalla et al. 1998; Williams et al. 1999).

²These equations contain the external pressure P_e . Equation (9) of Paper I allows us to solve for P_e , given the dimensional cloud mass M .

Lee, Myers, & Tafalla (1999) conducted the first largescale, systematic observations of N_2H^+ in starless dense cores. The 220 sources in their catalog had been selected primarily on the basis of optical obscuration. For the 72 objects detected in N_2H^+ , detailed study was made of the relatively isolated $F_1, F = 0, 1 \rightarrow 1, 2$ hyperfine line at 93.176 GHz. This line almost always has a Gaussian profile, with no self-absorption or asymmetry. The mean measured peak intensity was $T_A = 0.19 \pm 0.11$ K, and the FWHM was $\Delta V_{\text{N}_2\text{H}^+} = 0.35 \pm 0.14$ km s⁻¹. Lee, Myers, & Tafalla (2001) followed up these single-pointing observations with spatial maps of many individual cores. The N_2H^+ emission is compact, with a well-defined central peak. Diameters of the regions within the half-maximum contours range from 0.05 to 0.13 pc.

3.2. CS

These properties of N_2H^+ emission are in sharp contrast to those of the $J = 2 \rightarrow 1$ rotational line of CS at 97.981 GHz. Lee, Myers, & Tafalla (1999) found, in the 163 starless cores for which the line was detected, that a large fraction of the profiles were asymmetric and skewed toward the blue, either with two distinct peaks or, more commonly, a blue peak and a red shoulder (see their Figure 1). Detailed profiles vary from source to source, and there are even a few examples of double-peaked profiles stronger in the red. The subsequent mapping survey of Lee, Myers, & Tafalla (2001) showed that the region of CS asymmetry is relatively diffuse, and the emission is frequently depressed just where the N_2H^+ intensity peaks (see also Tafalla et al. 2002).

With both the optically thin (N_2H^+) and optically thick (CS) lines in hand, one may quantify the degree of blue-red asymmetry of the latter. Mardones et al. (1997) introduced δV_{CS} , the normalized velocity shift of CS. This quantity is defined as

$$\delta V_{\text{CS}} \equiv \frac{V_{\text{CS}} - V_{\text{N}_2\text{H}^+}}{\Delta V_{\text{N}_2\text{H}^+}}. \quad (3)$$

Here, V_{CS} and $V_{\text{N}_2\text{H}^+}$ are the peak, line-of-sight velocities of the two species. The peak velocity of N_2H^+ is assumed to represent the systematic motion of the cloud as a whole. In the single-pointing survey of Lee, Myers, & Tafalla (1999), δV_{CS} was usually negative, signifying that the profile peak is blueward of line center. The mean value of δV_{CS} in this sample was -0.24 ± 0.04 .

3.3. HCN

The $J = 1 \rightarrow 0$ rotational transition of HCN is the latest diagnostic tool for studying the kinematics of starless cores. As mentioned previously, the molecule suffers little depletion, at least for central densities less than 10^5 cm⁻³ (Aikawa et al, 2005). Integrated intensity maps show that the HCN emission region is roughly coextensive with that of N_2H^+ (Sohn et al. 2004). The $J = 1 \rightarrow 0$ transition consists of three hyperfine lines of differing optical depth: $F(0-1)$ at 88.634 GHz, $F(2-1)$ at 88.632 GHz, and $F(1-1)$ at 88.630 GHz. Under optically thin, LTE

conditions, these would have intensity ratios of 1 : 5 : 3. Of course, it is the fact that these lines are optically thick in starless cores that makes them useful kinematic probes.

Sohn et al. (2007) conducted single-pointing observations for HCN in 85 starless cores, netting 64 detections. The profiles of all three hyperfine lines are distinctly non-Gaussian, displaying either two peaks with a self-absorption dip or a single peak with a shoulder. Not surprisingly, the central dip is strongest in the optically thickest $F(2-1)$ line, which also shows the greatest blue-red asymmetry. But a central result of this study is the heterogeneity of the profiles. While 43 percent of the sources have at least one or two double-peaked hyperfine lines skewed to the blue, 33 percent have blueward and redward asymmetries mixed in the three lines.

Nevertheless, the overall tendency is for profiles indicative of contraction, rather than expansion. In analogy with equation (3), Sohn et al. (2007) defined δV_{HCN} , a normalized velocity shift with respect to N_2H^+ . For each hyperfine line, the large majority of sources are observed to have negative δV_{HCN} (see their Figure 4). The actual magnitudes of δV_{HCN} are larger than for CS. The mean values are -0.51 ± 0.06 , -0.41 ± 0.10 , and -0.59 ± 0.08 for $F(0-1)$, $F(2-1)$, and $F(1-1)$, respectively. Moreover, the magnitudes are tightly correlated, in the sense that a source with greater $|\delta V_{\text{HCN}}|$ in the $F(0-1)$ line also has a greater shift in $F(2-1)$ and $F(1-1)$. Within each source, however, there is no clear pattern for the relative magnitudes of the velocity shifts for the three lines, nor for the relative intensities of the lines. In other words, starless cores frequently exhibit HCN “intensity anomalies” with respect to LTE, a phenomenon that has long been noted and studied in other molecular clouds (e.g., González-Alfonso & Cernicharo 1993).

Because of the range in optical depths in the three lines, the profiles of HCN are potentially useful for tracing the full velocity structure of a dense core. Lee et al. (2007) constructed single-dish spatial maps of emission for two starless cores, L694-2 and L1197. To complement their observations, they also performed a radiative transfer calculation in spherical cloud models with adjustable density and velocity profiles. Interestingly, monotonic velocity profiles do not match the data. For both starless cores, Lee et al. (2007) found that the inferred contraction speed begins relatively small at the cloud edge, reaches a maximum about halfway inward in radius, and thereafter declines toward the cloud center. This type of velocity profile emerges naturally from our dynamical model (Paper I; Figure 4).

4. Numerical Results

4.1. Trends in Calculated Line Profiles

After setting the oscillation amplitude to $\epsilon = 0.1$, we next gauge how the line profiles, still viewed through the cloud center, change as the other parameters are varied. These trends enable us to seek a model whose lines best match the data in an average sense. Recall that our remaining free parameters are: κ , the turbulence coefficient in equation (1), the cloud mass M , and the time t

since the start of inward motion. The updated molecular abundances we used in the transfer code were: $X(\text{N}_2\text{H}^+) = 7 \times 10^{-10}$ (Benson, Caselli, & Myers 1998); $X(\text{CS}) = 4 \times 10^{-9}$ (Tafalla et al. 2002); and $X(\text{HCN}) = 3 \times 10^{-9}$ (Fuller et al. 1991; Li et al. 2004).

We first explored the effect of altering the cloud mass at fixed κ and t . Following Lee, Myers, & Tafalla (1999), we focused on the $F_1, F = 0, 1 \rightarrow 1, 2$ hyperfine line of N_2H^+ .³ As M is raised, the N_2H^+ line remains Gaussian, and is therefore still optically thin. Of course, the total emission increases with M , so that $\Delta V_{\text{N}_2\text{H}^+}$ also rises.

In CS and HCN lines exhibiting self-absorption, these dips eventually disappear with increasing cloud mass. This tendency is easy enough to understand. According to equation (2), an increase of M at fixed t necessitates a lower \tilde{t} . We are viewing our fiducial, contracting cloud at an earlier nondimensional time, when the cloud radius \tilde{r} was larger. But equations (9), (10), and (12) of Paper I imply that

$$M R^{-2} = \frac{\tilde{m} \tilde{t}}{\tilde{r}^2} \frac{a_T}{G t}. \quad (4)$$

Since \tilde{t}/\tilde{r}^2 falls, the column density through the cloud *decreases* with increasing M . Many observed lines, especially those of HCN, show clear self-absorption. Thus, the sensitivity of the calculated profiles effectively sets a ceiling on the allowable range of cloud masses.

A similar disappearance of the self-absorption dips in CS and HCN occurs when we fix M and t , but increase κ . A larger value of κ corresponds to a greater velocity dispersion throughout the cloud. The gas consequently has a higher, overall excitation temperature, so there is less of the absorption that creates central line dips. By the same token, the optically thin N_2H^+ line broadens, i.e., $\Delta V_{\text{N}_2\text{H}^+}$ increases. Both trends help us to set bounds on κ .

Finally, we may fix M and κ , and consider various evolutionary times t . At greater t , the maximum infall speed within the cloud increases. Thus, the blue/red asymmetry of all optically thick lines becomes more pronounced. Quantitatively, both δV_{CS} and δV_{HCN} which are both negative, become larger in magnitude. Figure 1 shows that the overall emission in N_2H^+ increases with time, a reflection of the higher cloud density. The line peak grows faster than its width, with the result that $\delta V_{\text{N}_2\text{H}^+}$ declines. In the figure, the FWHM is 0.24 km s^{-1} at the initial instant, and 0.21 km s^{-1} at the last time shown ($t = 1 \text{ Myr}$).

4.2. Canonical Model

Rather than attempt to find, within the model parameter space, matches to individual dense cores, we sought first a combination of M , t , and κ that reproduces the general, observed charac-

³The N_2H^+ table of LAMDA lists 3 lines at 93.176 GHz corresponding to the transitions $F_1, F = 0, 1 \rightarrow 1, 2$, $F_1, F = 0, 1 \rightarrow 1, 1$, and $F_1, F = 0, 1 \rightarrow 1, 0$. The lower levels are also listed as being degenerate in Table 1 of Daniel et al. (2005). Assuming the three individual lines cannot be resolved in practice, we added their intensities.

teristics of the various line profiles, as summarized in §3. Some experimentation was required, in light of the constraints just given. However, a suitable parameter set quickly emerged. If we set $M = 3 M_{\odot}$, $t = 1$ Myr, and $\kappa = 5.5 \times 10^{-12}$ g cm s⁻² (i.e., 0.5 times the original value found by Myers & Goodman (1988)), then the profiles are generally consistent with the data.

Following our previous discussion, it is the magnitude of the self-absorption dip that is most sensitive to variations in these parameters. We may accordingly gauge the acceptable range of parameter values by noting when the dips depart substantially from those in the canonical model. Holding t and κ fixed while allowing M to range from 2.7 to 3.2 M_{\odot} , the magnitude of the dip in the $F(2-1)$ line of HCN changed by less than 25 % in either direction. By the analogous measure, t can vary from 0.8 to 1.2 Myr, and κ from 3.3 to 8.8×10^{-12} g cm s⁻¹.

The topmost curve in Figure 1 shows the calculated N₂H⁺ profile for the canonical model. As in nearly all observed cases, the line is symmetric and Gaussian. Our FWHM of 0.21 km s⁻¹ is on the low end of the observed range, as would be expected given our assumed kinetic temperature of 10 K. Conversely, our T_A-value of 0.33 K is higher than the average. Here, of course, the beam efficiency (assumed to be unity in RATRAN) comes into play, as do the various distances to the observed dense cores.

Figure 2 (dashed curve) shows the emergent profile of CS through the center of the canonical cloud model. Because of higher optical depth, the line is markedly asymmetric, as the data also show. However, while the sense of the asymmetry in this calculated profile is correct, the deep, self-absorption dip is rarely seen (compare Figure 1 of Lee, Myers, & Tafalla (1999)). What is observed instead is a relatively broad, redshifted shoulder joining onto a blueshifted peak.

We may recover this shape by introducing depletion of the molecule, presumably caused by adsorption onto grain surfaces. Tafalla et al. (2002) invoked such depletion to improve the observational match of their CS spatial intensity maps. Following these authors, we assume a centrally depressed, radial profile for the relative number density:

$$X(r) = X_{\circ} \exp[-n(r)/n_d] . \quad (5)$$

Here, X_{\circ} is the usual interstellar value of X (CS), $n(r)$ is the cloud number density, and the threshold density n_d is a free parameter. For the solid profile in Figure 2, we used $n_d = 1 \times 10^4$ cm⁻³. As a comparison, Table 4 of Tafalla et al. (2002) lists n_d -values ranging from 1 to 5×10^4 cm⁻³ for five starless cores. Our calculated relative velocity shift, $\delta V_{\text{CS}} = -0.24$, is equal to the mean observed (Lee, Myers, & Tafalla 1999).

The three hyperfine lines of HCN (Figure 3) exhibit more diverse profile shapes. The optically thinnest $F(0-1)$ transition has a blue peak/red shoulder profile, similar to that in CS. The other two lines exhibit clear self-absorption, with the deepest trough being found in the optically thickest, $F(2-1)$ line. Scanning Figure 1 of Sohn et al. (2007), we see that this pattern is commonly seen (e.g., L63, L1197), but is by no means universal (e.g., L1544). Our calculated relative velocity shifts, δV , for the (0-1), (2-1), and (1-1) lines are -0.33, -0.81, and -0.67, respectively. As mentioned

earlier, observations give similar values for all three lines, with a mean of about -0.5. We are further encouraged by this qualitative agreement.

We stress that calculated line profiles are quite sensitive to the interior dynamics of the cloud, and thus do provide a worthwhile test of the underlying theory. To further illustrate this point, we recalculated all profiles using the collapse model of Shu (1977). We again set $t = 1 \times 10^6$ yr, where the zero of time now refers to the start of inside-out collapse. For $T = 10$ K, the mass of the central protostar in the model is $2 M_{\odot}$. In calculating profiles, we used the same velocity dispersion parameter, $\kappa = 5.5 \times 10^{-12}$ g cm s⁻², as in our canonical model.

All calculated line profiles are now far broader than those observed. For example, the N₂H⁺ profile, while remaining symmetric, is distinctly non-Gaussian, with a shallow, central depression and wings extending to ± 1 km s⁻¹ on either side of line center. Optically thick lines have profiles that are much too asymmetric. Our point here is *not* that the Shu model is a poor representation of starless cores, which was to be expected. The message is rather that the gas motions induced by a central protostar of solar-type mass are qualitatively different from those in our slowly contracting, starless cloud, and in a manner clearly reflected in the molecular line profiles.

4.3. Determining ϵ and t

Our canonical value of the oscillation amplitude ϵ , while guided by the scant observational data available, is still rather arbitrary. How, in the future, can we pin down this parameter when we examine specific dense cores? Even more importantly, will we be able to gauge the cloud's contraction age through comparison between real and model-generated line profiles?

These questions are related. We remarked in Paper I that an increase of ϵ , if accompanied by a *decrease* in the evolutionary time, could leave the cloud largely unchanged. If that were the case, it would be difficult to ascertain ϵ and t individually. Specifically, our cloud model, at a given ϵ and nondimensional time \tilde{t} , attains nearly the same contraction velocity as one at a different amplitude ϵ' and nondimensional time $\tilde{t}' = \tilde{t}(\epsilon/\epsilon')^2$. The nondimensional time scales as the inverse square of the amplitude because cloud contraction is driven by a second-order perturbation. The dimensional time may be obtained from the nondimensional one through equation (2). Does this scaling relation mean that line profiles are degenerate in ϵ and t ? Armed with RATRAN, we now demonstrate that this is fortunately not the case.

Figure 4 shows in detail the effect of trading amplitude and age. The solid curve in the lefthand panel is the velocity profile in our canonical model ($\epsilon = 0.1$; $t = 1$ Myr). The dashed curve is the profile for a cloud with the same mass of $3 M_{\odot}$, but with $\epsilon = 0.2$ and $t = 0.25$ Myr. As predicted, the velocities are quite similar. On the other hand, the internal *densities* differ greatly. The righthand panel shows that the cloud with larger ϵ has a lower central density, since it was initially more inflated and evolved over a shorter time.

The net result is that the line profiles also do not match. As an example, Figure 5 displays the three hyperfine lines of HCN. The degree of blue/red asymmetry in all the profiles is markedly less than in the canonical model. For the optically thinnest, $F(0-1)$ line, the profile is nearly Gaussian. The normalized velocity shift δV is only -0.16 km s^{-1} , well below typical observed values.

What happens if we keep $\epsilon = 0.2$, but increase t back to 1 Myr? For our model to be useful observationally, the resulting line profiles should again differ noticeably from the canonical case. Indeed they do, and in the opposite sense as the previous example. Both the CS and HCN profiles now exhibit *too much* asymmetry. For example, the red wing of the $F(0-1)$ line of HCN degenerates to a shoulder; a similar profile is seen in CS. According to Figure 1 of Myers, Evans, & Ohashi (2000), this development reflects relatively high infall speed. In fact, the maximum infall speed for this choice of parameters is 0.06 km s^{-1} , three times that in the canonical one. The central density is also higher by about the same factor. Consequently, the N_2H^+ line, while maintaining a Gaussian profile, has a T_A -value of 0.85 K, significantly above the range reported by Lee, Myers, & Tafalla (1999).

4.4. Abundance Gradients

We have seen that the calculated CS profile is not even qualitatively correct unless we include the effect of depletion onto grain surfaces. Our strategy, following previous authors, was simply to introduce a spatial variation in the molecular abundance. Nevertheless, our canonical model still assumes a uniform distribution of N_2H^+ and HCN. This simplification also bears examination.

The detailed abundance of any species is influenced not only by the efficiency of grain absorption but also by the cloud dynamics itself. The latter point was emphasized in the pioneering study by Rawlings & Yates (2001), who followed a time-dependent chemical reaction network in models of collapsing dense cores. Utilizing a radiative transfer code, these authors demonstrated, as we did in §4.2, the sensitivity of emergent molecular line profiles to the cloud’s internal velocity structure. Not only is there a direct, kinematic effect, but various species may not have time to achieve chemical equilibrium, creating abundance gradients that also influence line profiles. In a more recent work, Tsamis, Rawlings, Yates, & Viti (2008) found that the fractional abundance of N_2H^+ falls by an order of magnitude from cloud center to edge within a cloud undergoing inside-out collapse (see their Fig. 3).

To account fully for the interplay of dynamics and chemistry, we would also need to follow simultaneously both a chemical reaction network and line transfer in our evolving cloud model. Needless to say, such an undertaking is beyond the scope of this study. However, we may assess in a general way the effect of abundance gradients. Consider the optically thick lines of HCN, whose profiles should be especially sensitive. In the spirit of Tsamis, Rawlings, Yates, & Viti (2008), we adopt a linear variation of the relative HCN abundance:

$$X = X_{\circ} [1 + \beta (M_r/M - 1/2)] . \quad (6)$$

Here, M_r is the mass contained within any radius r and X_\odot is the nominal abundance we used previously. Within our canonical model, we vary the nondimensional slope β and calculate the emergent HCN profiles.

The slope β cannot exceed 2 in absolute value, since X would then become negative at either the cloud center or edge. For smaller, but substantial, values of $|\beta|$, the most significant effect is on the depth of the self-absorption dip. Figure 6 shows how the optically thickest, $F(2-1)$, line profile changes as β ranges from -0.5 through 0 (uniform abundance), to +0.5. According to the standard gauge of the relative velocity shift, the effect is minor. For $\beta = -0.5$, δV_{HCN} is 6 % greater in magnitude than the canonical value, while the shift is 6 % less for $\beta = +0.5$.

Nevertheless, the degree of self-absorption diminishes markedly for positive β , i.e., when HCN is concentrated in the more slowly moving, outer portion of the cloud. To restore the dip to its original magnitude, the contraction age for the cloud would need to increase slightly from the canonical 1.0 Myr to 1.2 Myr. We conclude that, while coupled chemical and dynamical models are preferable in principle, such extensive effort is unnecessary for beginning a quantitative assessment of starless core properties.

5. Discussion

This suite of radiative transfer calculations performed on our theoretical cloud model has yielded two important findings. First, we have been able to match the generic, observed properties of the selected line profiles using a reasonable cloud mass, turbulent velocity dispersion, and evolutionary time. This success may indicate that the model has captured the essential physics of the contraction process itself. Note also that the accelerating character of the contraction in our theory explains naturally the key observation that starless cores of lower density exhibit less asymmetry in their line profiles (Gregersen & Evans 2000; Williams, Lee, & Myers 2006). Second, the sensitivity of the emergent line profiles to the input parameters means that the model offers a practical route to gauge starless core properties that have previously been difficult to ascertain. For example, given the empirical mass and kinetic temperature of an object, the matching of line profiles would yield a first estimate of its contraction age. Obtaining ages for numerous starless cores in different environments would aid greatly in understanding the onset of star formation.

Of course, the observations offer more detail than the model can explain, at least in its current, highly idealized form. We cannot yet account for the rather surprising spatial extent of asymmetric CS emission (Myers, Evans, & Ohashi 2000; Lee, Myers, & Tafalla 2001). Nor can we explain the relative intensities of the HCN hyperfine lines (Sohn et al. 2004). Explaining both features of the data may require alterations in the spatial abundance gradients, in the manner employed in Sections 4.2 and 4.4. Additionally, an improved model would consider more carefully how the interior, relatively quiescent gas joins onto surrounding, more turbulent, material. In fact, it has long been realized that the pattern of HCN hyperfine anomalies requires the presence of an envelope

of relatively high excitation temperature (González-Alfonso & Cernicharo 1993). Gong & Ostriker (2009) have recently simulated the birth of dense cores out of spherical, converging flows. Such calculations, when extended to three dimensions, may offer additional insight into the nature of the core-envelope transition.

Finally, we must face the obvious fact that real starless cores are not spherical, as the model currently assumes. The shapes of these objects may be partially determined by the anisotropic pressure of their turbulent environments, as found in recent simulations (e.g. Offner, Klein, & McKee 2008). Another important factor setting the gross core properties is the force associated with the internal magnetic field (Li et al. 2004). It would be instructive to study, using the method of Paper I, the onset of collapse in marginally stable, magnetostatic equilibria, such as those found by Tomisaka, Ikeuchi, & Nakamura (1988). Such an investigation would add a significant degree of realism to our picture of protostellar collapse.

We are grateful to Floris van der Tak, one of the authors of RATRAN, for guiding us in the proper use of the code. Jorge Piñeda, who is independently analyzing the line emission from cloud models, also provided much-valued assistance, as did Melissa Enoch. Throughout the project, S. S. was partially supported by NSF grant AST-0908573.

REFERENCES

- Aikawa, Y., Herbst, E., Roberts, H., & Caselli, P. 2005, *ApJ*, 620, 330
- Barranco, J. A. & Goodman, A. A. 1998, *ApJ*, 504, 207
- Benson, P. J., Caselli, & Myers, P. C. 1998, *ApJ*, 506, 743
- Caselli, P., Benson, P. J., Myers, P. C., & Tafalla, M. 2002, *ApJ*, 572, 238
- Bergin, E. A. & Langer, W. D. 1997, *ApJ*, 486, 316
- Broderick, A. E., Keto, E., Lada, C. J., & Narayan, R. 2007, *ApJ*, 671, 1832
- Caselli, P., Myers, P. C. & Thaddeus, P. 1995, *ApJ*, 455, L77
- Cilek, G. & Basu, S. 2001, *ApJ*, 547, 272
- Crapsi, A., Caselli, P., Walmsley, C. M., Myers, P. C., Tafalla, M., Lee, C. W., & Bourke, T. L. 2005, *ApJ*, 619, 379
- Daniel, F., Dubernet, M.-L., Meuwly, M, Cernicharo, J., & Pagine, L. 2005, *MNRAS*, 363, 1083
- Forbrich, J., Lada, C. J., Muench, A. A., Alves, J., & Lombardi, M. 2009, *ApJ*, 704, 292
- Fuller, G. A. 1989, Ph.D. thesis, U. of California, Berkeley
- Fuller, G. A., Myers, P. C., Welch, W. J., Goldsmith, P. F., Langer, W. D., Campbell, B. G., Guilloteau, S., & Wilson, R. W. 1991, *ApJ*, 376, L35
- Gong, H. & Ostriker, E. C. 2009, *ApJ*, 699, 230
- González-Alfonso, E. & Cernicharo, J. 1993, *A&A*, 279, 506
- Gregersen, E. M. & Evans, N. J. 2000, *ApJ*, 538, 260
- Hogerheijde, M. R. & van der Tak, F. F. S. 2000, *A&A*, 362, 697
- Hunter, C. 1997, *ApJ*, 218, 834
- Jijins, J., Myers, P. C. & Adams, F. C. 1999, *ApJS*, 125, 161
- Keto, E. & Caselli, P. 2008. *ApJ*, 683, 238
- Keto, E. & Field, G. 2005, *ApJ*, 635, 1151
- Keto, E., Broderick, A. E., Lada, C. J., & Narayan, R. 2006, *ApJ*, 652, 1366
- Kirk, H., Johnstone, D., & Di Francesco, J, 2006, *ApJ*, 646, 1009

- Larson, R. B. 1969, MNRAS, 145, 271
- Lee, J.-E., Bergin, E. A., & Evans, N. J. 2004, ApJ, 617, 360
- Lee, C. W. & Myers, P. C. 1999, ApJS, 123, 233
- Lee, C. W., Myers, P. C., & Tafalla, M. 1999, ApJ, 526, 788
- Lee, C. W., Myers, P. C., & Tafalla, M. 2001, ApJS, 136, 703
- Lee, S. H., Park, Y.-S., Sohn, J., Lee, C. W., & Lee, H. M. 2007, ApJ, 660, 1326
- Li, P. S., Norman, M. L., Mac Low, M.-M., & Heitsch, F. 2004, ApJ, 605, 800
- Lizano, S. & Shy, F. H. 1989, ApJ, 342, 834
- Mardones, D., Myers, P. C., Tafalla, M., Wilner, D. J., Bachiller, R., & Garay, G. 1997, ApJ, 489, 719
- Myers, P. C., Evans, N. J., & Ohashi, N. 2000, in Protostars and Planets IV, ed. V. Mannings, A. P. Boss, & S. S. Russell, Tuscon: U. of Arizona, 217
- Myers, P. C. & Goodman, A. A. 1998, ApJ, 329, 392
- Myers, P. C., Mardones, D., Tafalla, M., Williams, J. P., & Wilner, D. J. 1996, ApJ, 465, L133
- Offner, S., Klein, R. I., & McKee, C. F. 2008, ApJ, 686, 1174
- Penston, M. V. 1969, MNRAS, 144, 425
- Rawlings, J. M. C. & Yates, J. A. 2001, MNRAS, 326, 1423
- Redman, M. P., Keto, E., & Rawlings, J. M. C. 2006, MNRAS, 370, L1
- Rybicki, G. B. & Hummer, D. G. 1991, A&A, 245, 171
- Sault, R. J., Teuben, P. J., & Wright, M. C. H. 1995, Astronomical Data Analysis and Software Systems IV, 77, 433
- Schnee, S., Caselli, P., Goodman, A., Arce, H. G., Ballesteros-Paredes, J., & Kuchibhotla, K. 2007, ApJ, 671, 1839
- Shöier, F. L., van der Tak, F. F. S., van Dishoeck, E. F., & Black, J. H. 2005, A&A, 432, 369
- Shu, F. H. 1977, ApJ, 214, 498
- Sohn, J., Lee, C. W., Lee, H.-M., Park, Y.-S., Myers, P. C., Lee, Y., & Tafalla, M. 2004, J. Korean Astron. Soc., 37, 261
- Sohn, J., Lee, C. W., Park, Y.-S., Lee, H.-M., Myers, P. C., & Lee, Y. 2007, ApJ, 664, 928

- Stahler, S. W. & Yen, J. J. 2009, MNRAS, 396, 579
- Tafalla, M., Mardones, D., Myers, P. C., Caselli, P., Bachiller, R., & Benson, P. J. 1998, ApJ, 504, 900
- Tafalla, M., Myers, P. C., Caselli, P., Walmsley, C. M., & Comito, C. 2002, ApJ, 569, 815
- Tomisaka, K., Ikeuchi, S., & Nakamura, T. 1988, ApJ, 335, 239
- Tsamis, Y. G., Rawlings, J. M. C., Yates, J. A., & Viti, S. 2008, MNRAS, 388, 898
- Turner, B. E. & Thaddeus, P. 1977, ApJ, 211, 755
- Velusamy, T., Peng, R., Li, D., Goldsmith, P. F., & Langer, W. D. 2008, ApJ, 688, L87
- Walker, C. K., Lada, C. J., Young, E. T., Maloney, P. R., & Wilking, B. A. 1986, ApJ, 309, L47
- Williams, J. P., Myers, P. C., Wilner, D. J., & Di Francesco, J. 1999, ApJ, 513, L61
- Williams, J. P., Lee, C. W., & Myers, P. C. 2006, ApJ, 636, 953
- Womack, M., Ziurys, L. M., & Wyckoff, S. 1992, ApJ, 387, 417
- Zhou, S. 1992, ApJ, 394, 204

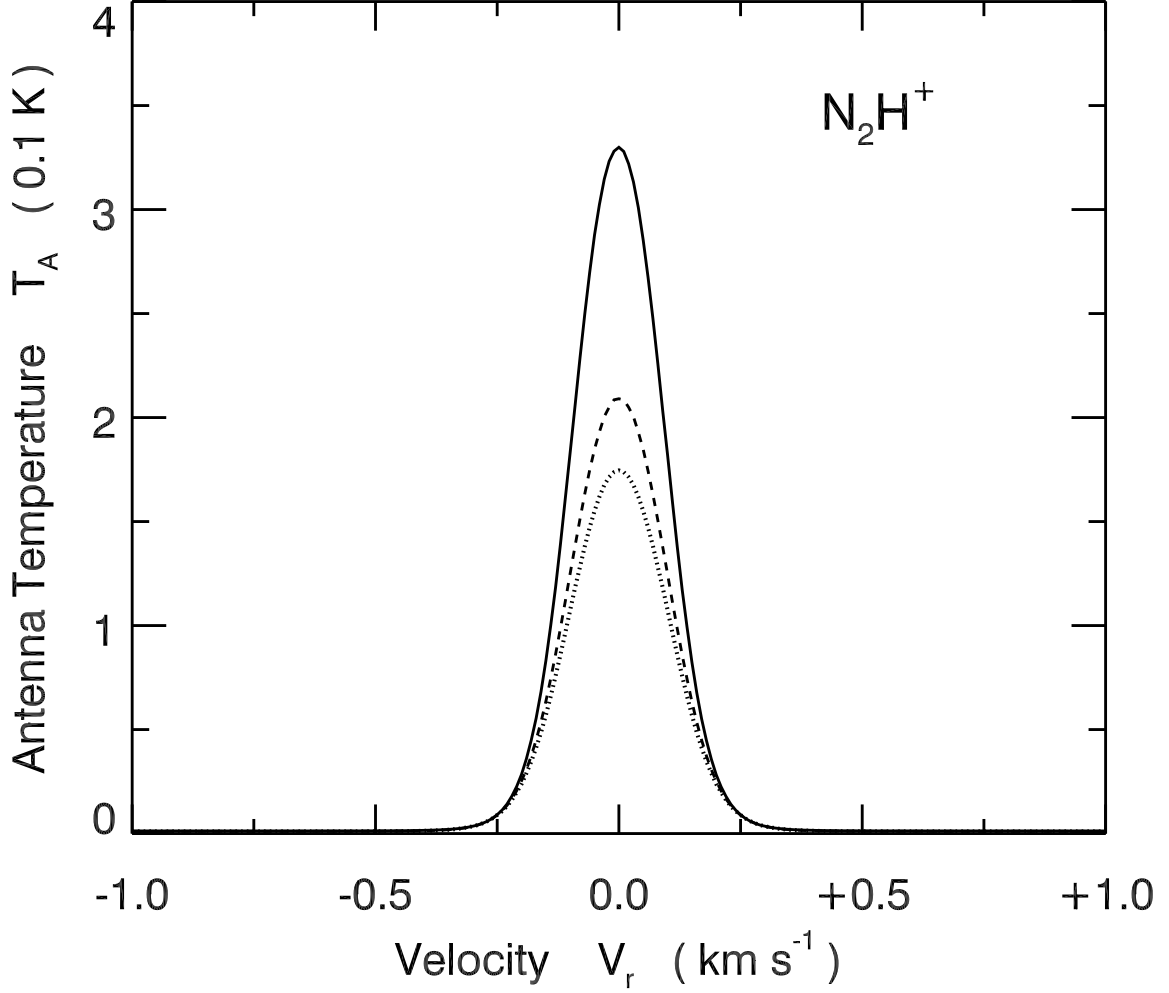


Fig. 1.— Profile evolution of the $F_1, F = 0, 1 \rightarrow 1, 2$ hyperfine line within the $J = 1 \rightarrow 0$ rotational transition of N_2H^+ . The profiles, viewed through the cloud center, are for a cloud of $3 M_\odot$ with $\kappa = 5.5 \times 10^{-12} \text{ g cm}^{-1} \text{ s}^{-2}$. From bottom to top, the times are 0, 0.5, and 1.0 Myr.

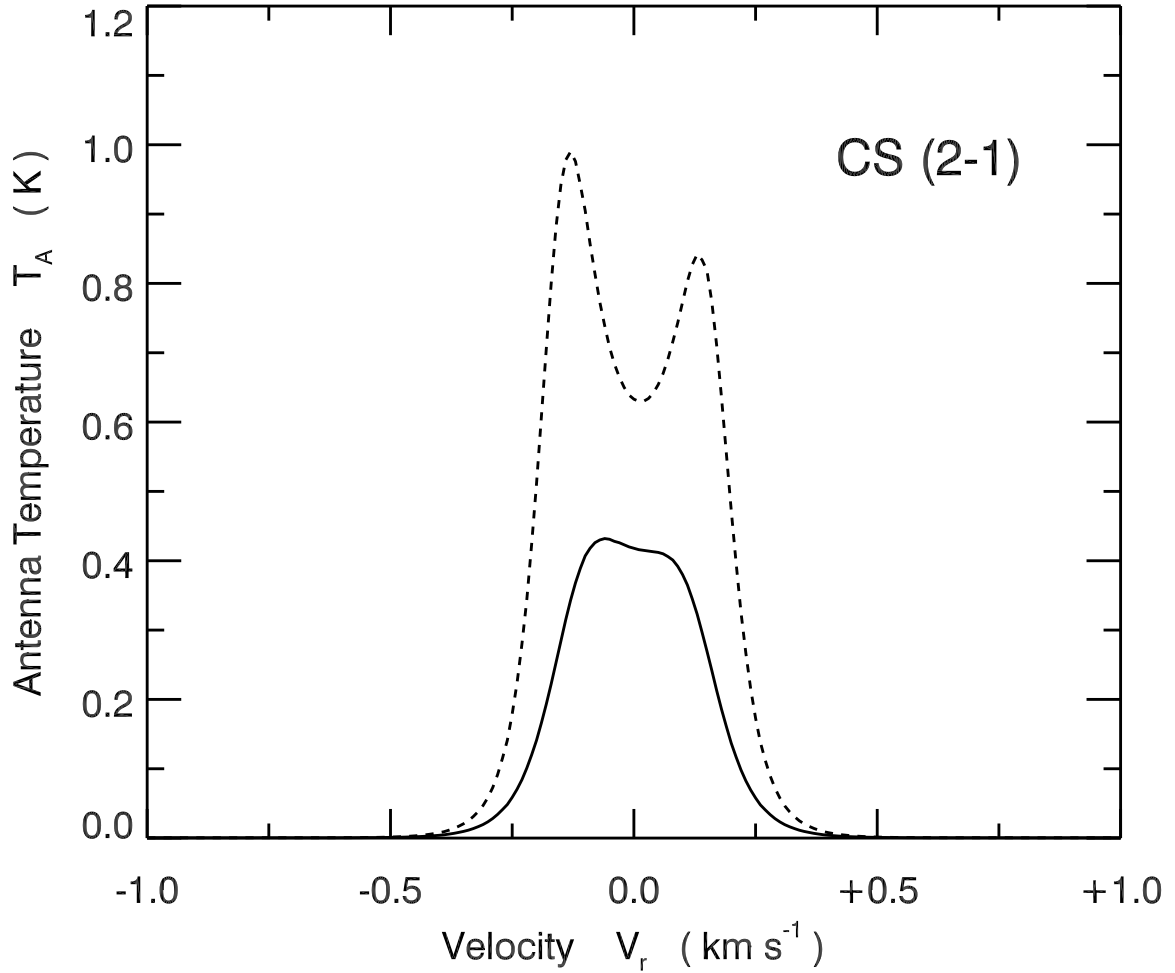


Fig. 2.— Profile of the $J = 1 \rightarrow 0$ rotational transition of CS, viewed through the cloud center for the canonical cloud model. The dashed curve is the profile using a uniform CS relative abundance of $X(\text{CS}) = 4 \times 10^{-9}$. For the solid profile, the molecule was centrally depleted, following the prescription of Tafalla et al. (2002).

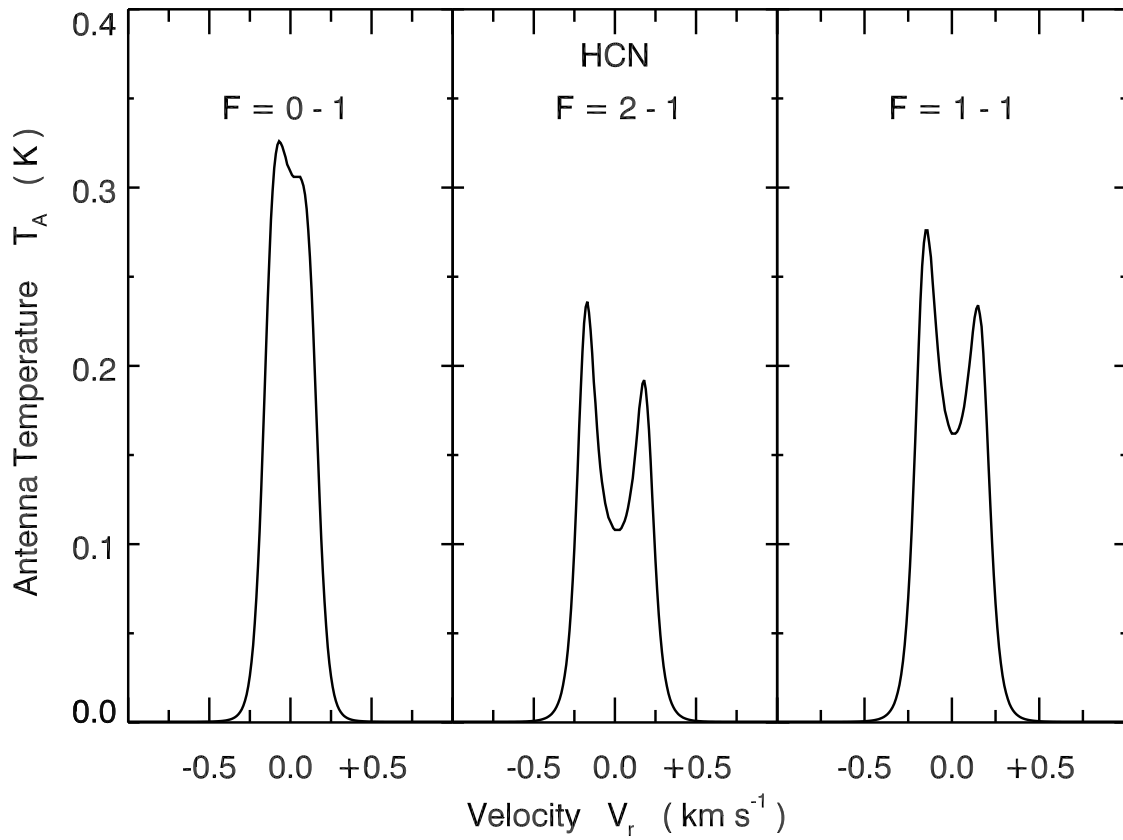


Fig. 3.— Profiles of HCN for the three hyperfine lines within the $J = 1 \rightarrow 0$ rotational transition. All profiles are calculated using the canonical model, and are viewed through the cloud center.

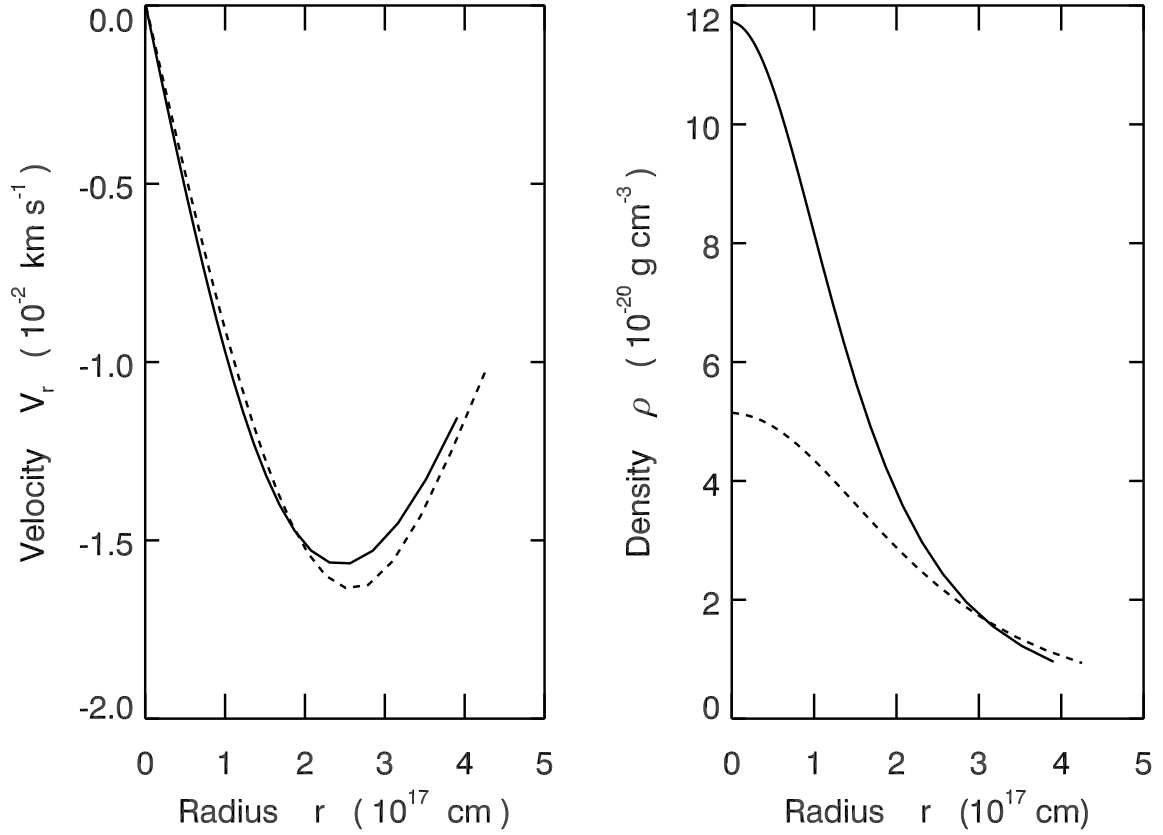


Fig. 4.— Theoretical velocity and density profiles. The left panel shows the contraction velocity as a function of radius. The solid curve is the canonical model ($\epsilon = 0.1$, $t = 1$ Myr), while the dashed curve has $\epsilon = 0.2$ and $t = 0.25$ Myr. The right panel displays the density profiles for the same two models.

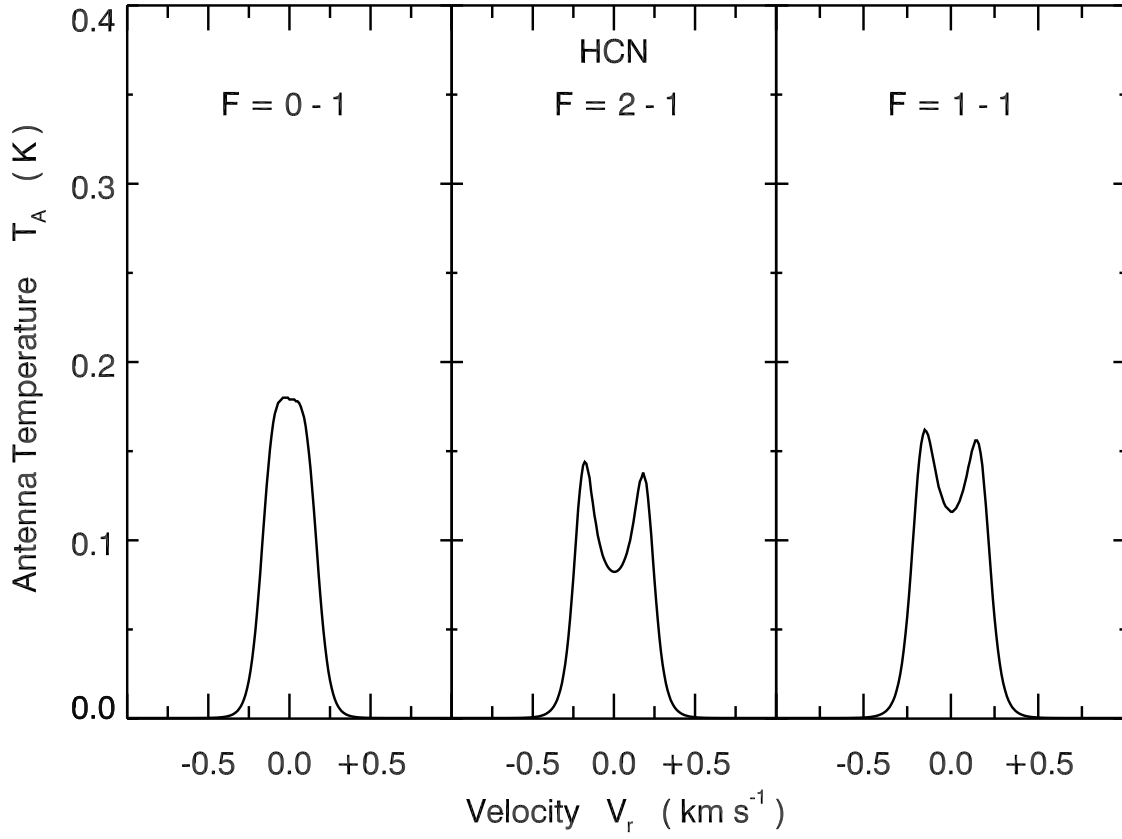


Fig. 5.— The effect of changing ϵ and t on the three hyperfine lines of HCN. All profiles are calculated using $\epsilon = 0.2$ and $t = 0.25$ Myr, and are viewed through the cloud center. Note how the asymmetry is decreased with respect to the profiles of Figure 3.

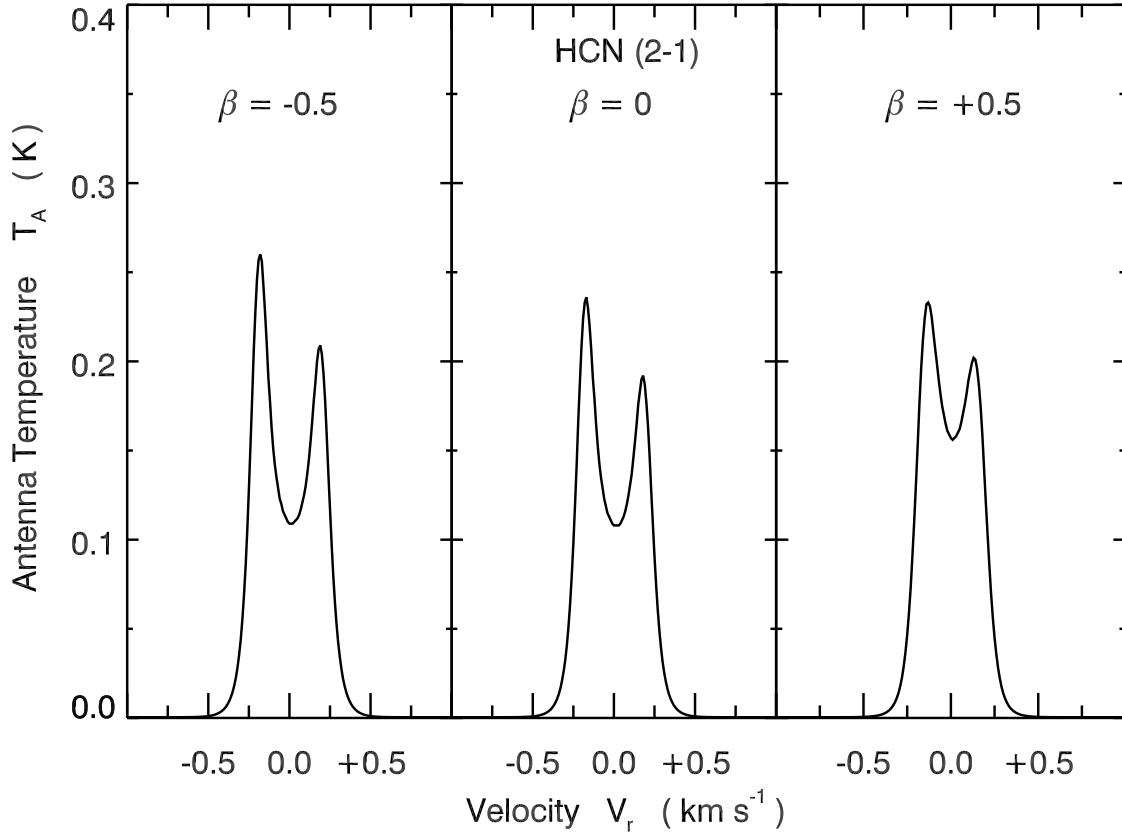


Fig. 6.— The effect of abundance gradients on the $F(2-1)$ HCN hyperfine line. The cloud model is the canonical one, with the addition of a linear HCN abundance gradient. The slope β , as defined in equation (6) is given in each panel. Notice how the self-absorption dip decreases for positive β .